

Pairing insights in iron-based superconductors from scanning tunneling microscopy

Can-Li Song, Jennifer E. Hoffman

Department of Physics, Harvard University, Cambridge, MA 02138, U. S. A.

Abstract

Scanning tunneling microscopy (STM) has made tremendous progress in the study and understanding of both classical and unconventional superconductors. This has motivated a rapidly growing effort to apply the same techniques to the iron-based high- T_c superconductors since their discovery in 2008. Five years have brought exciting advances in imaging and spectroscopic investigation of this new class of materials. In this review, we focus on several recent STM contributions to the identification of the gap symmetry and pairing glue. We highlight the unique capabilities and challenges still ahead for STM studies of iron-based superconductors.

Keywords: Scanning tunneling microscopy, Iron-based superconductors, Pairing symmetry

1. Introduction

Magnetism has long been thought to be antagonistic to superconductivity. Therefore, the 2008 discovery of superconductivity in iron-containing $\text{LaO}_{1-x}\text{F}_x\text{FeAs}$ [1], with transition temperature T_c rapidly climbing to 55 K upon replacement of La by magnetic rare earth elements [2], was unexpected and provoked worldwide excitement. As in the case of cuprates, the superconductivity emerges from the antiferromagnetic parent compounds, suggesting a link between spin fluctuations and electron pairing in both materials [3]. This finding opens a new avenue to address the two ultimate goals in the field of superconductivity: to seek the microscopic origin of the high T_c and then design new materials with higher T_c . Despite extensive experimental and theoretical explorations, iron-based superconductors (Fe-SCs) still face fierce debates on a number of issues including gap symmetry, a prerequisite for understanding the secret of high- T_c superconductivity. An excellent review by Johnston has thoroughly discussed the puzzle in Fe-SCs through 2010 [4]. Another comprehensive review by Stewart covers the rapidly-moving field through 2011 [5].

Scanning tunneling microscopy (STM) provides unique capabilities to image the atomic and electronic structure of a surface with a sub-unit-cell spatial

resolution. STM has been applied with great success to the study of conventional and cuprate superconductors [6]. The local density of states directly measured by STM spectroscopy provides indispensable information about the superconducting gap structure, its spatial inhomogeneity and behaviors near impurity as well as vortex core states. Furthermore, via quasiparticle interference (QPI) imaging, STM can provide momentum-resolved information about pairing symmetry, collective excitations, and competing phases. All these accomplishments motivate the growing use of STM to study Fe-SCs in the quest to understand the intricate electron pairing in these materials.

Following an early review of STM studies of Fe-SCs by Yin *et al* [7], STM has made considerable new progress and greatly contributed to the study of some of the most unusual and remarkable properties of these materials. A more thorough review by Hoffman recently discussed the cleaved surface configurations, superconducting and other spectral gaps, and vortex states [8]. Our new review here will begin with a brief introduction to the STM technique in section 2, then concentrate on the experimental highlights in the pairing symmetry of Fe-SCs obtained over the past year by STM, such as tunneling spectroscopy in section 3, QPI in section 4, and vortex state in section 5. In section 6, we conclude by mentioning a few very recent hints of higher T_c in iron-based materials, as well as suggestions for future STM experiments that should shed additional

*Corresponding author: jhoffman@physics.harvard.edu

light on these materials.

2. Scanning tunneling microscopy and spectroscopy

STM is based on the quantum tunneling of electrons between two electrodes separated by a thin potential barrier. A sharp metallic tip, which acts as a local probe, is brought within a short distance (typically several Å) of an electrically conducting sample surface. The tip can be positioned with sub-Å precision in both the xy plane and the z direction using a three-dimensional piezoelectric scanner, as schematically illustrated in Fig. 1(a). Applying a bias voltage between the metallic tip and conducting sample leads to a measurable tunneling current; the polarity of the bias voltage determines the direction of the net electron flow. For instance, a negative bias voltage applied to the sample will allow electrons to tunnel from the occupied states of the sample through the vacuum barrier into the empty states of the tip [Fig. 1(b)]. Upon reversing the bias polarity, the electrons will tunnel in the opposite direction, from occupied states of the tip into empty states of the sample. Based on the Tersoff-Hamann theory [9], the tunneling current I can be well approximated by

$$I \propto e^{-2\kappa d}, \quad \kappa = \frac{\sqrt{2m\phi}}{\hbar} \approx 0.5 \sqrt{\phi} \text{ \AA}^{-1} \quad (1)$$

where ϕ is a mixture of the work functions of the tip and sample measured in eV and d is the tip-sample separation measured in Å. For typical metals, $\phi \sim 5$ eV, so I will increase by about one order of magnitude for every Å decrease in d .

In topographic mode, the surface is mapped based on the decay of tunneling current I with increasing tip-sample separation d . With the bias voltage V fixed, the error signal between the measured current I_{meas} and the setpoint current I_{set} is fed back to the z piezo to control d as the tip is rastered across the sample surface [Fig. 1(a)]. The z trajectory of the tip therefore maps a contour of constant integrated electron density of states (DOS). This technique is referred as constant-current mode. In the case of homogeneous DOS, the contour corresponds to the geometric topography of the surface. However, if the DOS varies spatially, the resulting image contains a mixture of DOS and geometric information. By setting the tunneling voltage V_{set} far from the energy range of spatially inhomogeneous states, the contribution of the inhomogeneous DOS can be significantly reduced, so

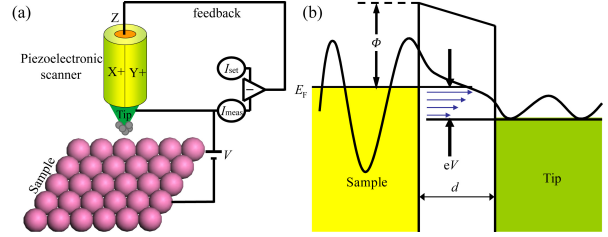


Figure 1: (color online) (a) Schematic of an STM. A voltage V is applied between a sharp metallic tip and a conducting sample surface, leading to a measurable tunneling current I_{meas} which decays exponentially with tip-sample separation d . In standard constant-current topographic imaging, the difference (or the error signal) between I_{meas} and the setpoint current I_{set} is fed back to the z piezo to control the tip height. (b) Tunneling process of electrons between the tip and sample across a vacuum barrier of width d and height ϕ . The electron wave functions of both the sample and tip decay exponentially into vacuum with a small overlap, allowing electrons to tunnel between them. With a negative bias voltage V applied to the sample, electrons tunnel from the occupied states of the sample to the empty states of the tip.

that geometry will dominate the topographic image as desired.

In addition to revealing the geometry of a sample surface, STM can also probe the evolution of sample DOS with energy, up to several eV from the Fermi level (E_F) in both occupied and unoccupied states. The DOS can be accessed by switching off the feedback circuit to fix d , sweeping the bias voltage V , and recording the tunneling current $I(V)$. The conductance dI/dV can be obtained either by numerical differentiation of $I(V)$ or by a lock-in amplifier technique. In the latter case, a small modulation is added to the bias voltage V , and the tunneling current I is demodulated to yield dI/dV . Although the interpretation of dI/dV spectra can be quite complex, in ideal conditions dI/dV is a good measure of the sample DOS. If these dI/dV spectra are recorded on a dense array of locations in real space with well-chosen V_{set} , the spatial variation of the sample DOS can be extracted. This DOS mapping technique has been applied to measure local gap variations and magnetic vortices [6, 7, 8].

3. Tunneling spectroscopy

Like cuprates, all Fe-SCs are layered compounds. Most can be mechanically cleaved to expose an atomically flat and clean ab -surface, suitable for characterization by surface-sensitive probes. To date, STM spectroscopy techniques have revealed a wide distribution of reduced gap values $2\bar{\Delta}/k_B T_c$ across materials [8], varying degrees of gap inhomogeneity

within materials (inhomogeneous doped AFe_2As_2 [10, 11, 12] vs. homogeneous LiFeAs and FeSe [13, 14]), multiple superconducting gaps within a single material due to the multi-band electronic structure [12], non-universal pairing gap symmetry [14, 15], and symmetry breaking in both superconducting and parent phases [14, 16, 17]. Here, we extend the discussion of pairing and normal state symmetry based on recent results from higher energy conductance features, atomic impurity imaging, and normal state spectroscopy.

3.1. Electron-boson coupling

Collective modes, which couple strongly to electrons and may serve as “glue” for Cooper pairing, often appear as additional conductance features at energies beyond the superconducting gap. This higher energy structure was first observed and quantitatively analyzed in conventional superconductor Pb-insulator-Pb tunnel junctions, where minimum in dI^2/dV^2 at positive energy $\Omega + 2\Delta$ was found to correspond to phonon mode energy [18]. However, the exact shape of the dI^2/dV^2 spectrum should be computed from a k -space integral involving the pairing gap, electron density of states, and density of states of the phonon (or other collective mode). In unconventional cuprates and Fe-SCs, the asymmetric electron pairing, complex Fermi surface and multi-band coupling complicate the calculation and preclude any universal relationship between the mode energy Ω and a regular feature of dI^2/dV^2 . Therefore, in different materials, Ω has been inconsistently extracted from several features in dI/dV or dI^2/dV^2 .

Tunneling experiments on cuprates showed a similar dip-hump structure in dI/dV at energies above the gap, and several studies [6, 19, 20, 21, 22] specifically matched the spectral features to the energy of a spin resonance mode Ω_r near (π, π) observed by neutron scattering [23, 24]. This supports the importance of spin fluctuations in the pairing mechanism of high- T_c cuprates [3].

Soon after the discovery of Fe-SCs, the importance of spin fluctuations was suggested in these materials as well, with the proposal that the high- T_c superconductivity arises through spin flip quasiparticle excitations between the Γ -centered hole pockets and M -centered electron pockets (so-called s_{\pm} wave pairing) [25, 26]. In this context, tunneling spectroscopy is again a powerful method to measure the energies of collective modes coupling to electrons, and to compare these energies to spin resonance modes detected by other techniques.

Fasano *et al* first observed a dip-hump feature by spectroscopic STM in nearly optimally doped

1111-type $\text{SmFeAsO}_{0.8}\text{F}_{0.2}$ ($T_c = 45$ K) [Fig. 2(a)], and argued that this feature was likely a spin resonance mode [27]. The spectral asymmetry makes it difficult to observe the superconducting gap edge and dip-hump structure on the negative energy (filled states) side, similar to early cuprate studies [19], which were later clarified with higher resolution spectra showing features at both polarities [20]. In $\text{SmFeAsO}_{0.8}\text{F}_{0.2}$ on the positive energy side (empty states), the energy of the presumed collective mode, $\Omega = E_{\text{dip}} - \Delta$, ranges from ~ 2 -8 meV, and locally anti-correlates with the presumed pairing strength Δ . This phenomenology is similar to the local anti-correlation of the presumed phonon [28] and spin resonance [22] mode energies with gap energies observed in cuprates. However, $\Omega = E_{\text{dip}} - \Delta \sim (0.5\text{-}2)k_B T_c$ (and even the larger $E_{\text{hump}} - \Delta \sim (2\text{-}3)k_B T_c$) are much lower than the universal neutron resonance energies $\Omega_r \sim 4.4k_B T_c$ found in Fe-SCs [29]. It is possible that surface contamination played a role in this study of uncleaned $\text{SmFeAsO}_{0.8}\text{F}_{0.2}$.

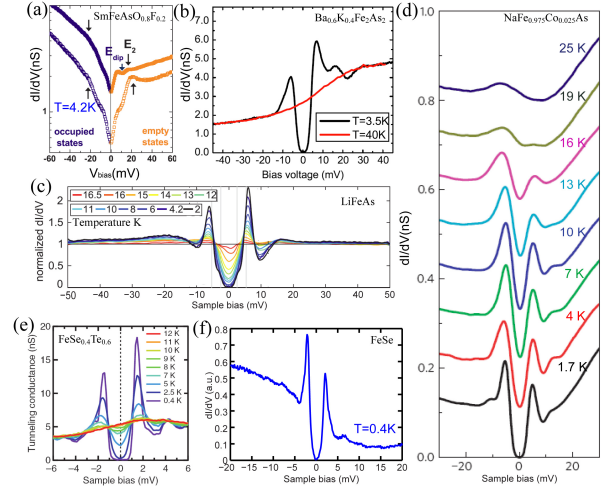


Figure 2: Large-energy-scale tunneling conductance spectra showing the dip-hump structure beyond the superconducting gaps in various Fe-SCs: (a) $\text{SmFeAsO}_{0.8}\text{F}_{0.2}$ ($T_c = 45$ K) [27]; (b) $\text{Ba}_{0.6}\text{K}_{0.4}\text{Fe}_2\text{As}_2$ ($T_c = 38$ K) [30]; (c) LiFeAs ($T_c = 17$ K) [31]; (d) $\text{NaFe}_{0.975}\text{Co}_{0.025}\text{As}$ ($T_c = 21$ K) [29]; (e) $\text{FeSe}_{0.4}\text{Te}_{0.6}$ ($T_c = 14.5$ K) [15]; (f) FeSe ($T_c = 9.3$ K) [14].

Shan *et al* subsequently reported a spectroscopic STM study of hole-doped 122-type $\text{Ba}_{0.6}\text{K}_{0.4}\text{Fe}_2\text{As}_2$ ($T_c = 38$ K) [30], in which features of a collective mode were more clearly visible beyond the superconducting gap in raw dI/dV spectra below T_c [Fig. 2(b)]. The mode energy of $\Omega \approx 13$ -14 meV, calculated as the difference between the dI^2/dV^2 minimum at the positive voltage and the larger superconducting gap $\Delta \approx 8.4$ meV, closely agrees with the spin resonance excitation $\Omega_r \approx$

14 meV as measured by neutron scattering [32]. Again, Ω anti-correlates locally with Δ within this material, which contrasts with the global positive correlation between spin resonance excitation Ω_r and T_c across 6 different Fe-SCs [29]. Balatsky *et al* addressed this same discrepancy in cuprates, proposing a local strong coupling model, where $\Delta(r)$ not only scales linearly with the boson mode energy $\Omega(r)$, but also correlates exponentially with the boson coupling constant $g(r)$ via $\Delta(r) \sim \Omega(r)e^{-1/g(r)}$ [33]. In other words, $g(r)$ is more important than $\Omega(r)$ in determining $\Delta(r)$. In addition, it was found that the effective coupling constant is inversely proportional to the boson energy $\Omega(r)$. Therefore, larger $\Omega(r)$ corresponds to weaker coupling $g(r)$, and consequently to smaller $\Delta(r)$.

To round out the four major families of Fe-SCs, Chi *et al* observed the dip-hump feature in 111-type stoichiometric LiFeAs ($T_c = 17$ K) [Fig. 2(c)] [31], and Wang *et al* observed the feature in slightly Co-doped NaFe_{0.975}Co_{0.025}As ($T_c = 21$ K) single crystals [Fig. 2(d)] [29]. Both the deduced bosonic mode energies, $\Omega = 5$ meV in LiFeAs and $\Omega = 7.8$ meV in NaFe_{0.975}Co_{0.025}As, are close to the spin resonance excitation $\Omega_r \approx 8$ meV [34]. Moreover, such features are also visible in dI/dV spectroscopy on 11-type iron chalcogenides FeSe_{0.4}Te_{0.6} ($T_c = 14.5$ K) [15] and FeSe ($T_c = 9.3$ K) [14] [Figs. 2(e) and 2(f)], although not clearly explained in these papers.

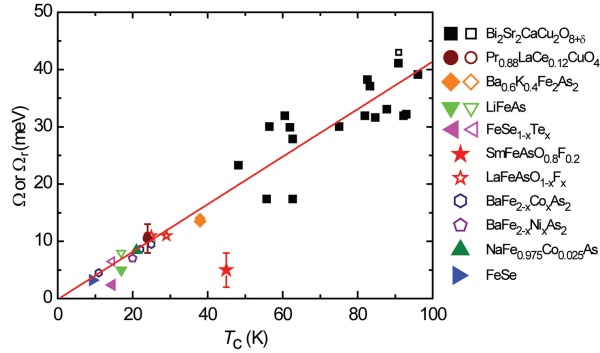


Figure 3: Collective resonance mode energy Ω from STM (filled symbols) and spin resonance Ω_r from neutron scattering (open symbols) in both cuprates and Fe-SCs vs. bulk T_c . The Ω data for Bi₂Sr₂CaCu₂O_{8+ δ} comes from dI/dV spectra from 17 different SIS break junctions at various hole dopings, and is computed as $\Omega = E(\text{dip in } dI/dV) - 2\Delta$ [21]. All other Ω data comes from STM junctions with normal state tips. Pr_{0.88}LaCe_{0.12}CuO₄: $\Omega = E(\text{peak in } dI^2/dV^2) - \Delta$ [22]; SmFeAsO_{0.8}F_{0.2}: $\Omega = E(\text{dip in } dI/dV) - \Delta$ [27]; Ba_{0.6}K_{0.4}Fe₂As₂: $\Omega = E(\text{dip in } dI^2/dV^2) - \Delta$ [30]; LiFeAs: $\Omega = E(\text{dip in } dI/dV) - \Delta$ [31]; NaFe_{0.975}Co_{0.025}As: $\Omega = E(\text{dip in } dI^2/dV^2) - \Delta$ [29]; FeSe_{0.4}Te_{0.6} and FeSe: $\Omega = E(\text{peak in } dI^2/dV^2) - \Delta$ [14, 15]. Neutron scattering data comes from Refs. [23, 24, 29, 32, 34].

Figure 3 summarizes the bosonic mode energy Ω derived from STM measurements and Ω_r from neutron scattering, in both cuprates and Fe-SCs, vs. the superconducting transition temperature T_c . Although T_c changes by a full order of magnitude, it is remarkable that most data collapse onto the universal relation Ω (or Ω_r)/ $k_B T_c = 4.8 \pm 0.3$. Furthermore, $\Omega/2\Delta < 1$ holds in both cuprates and Fe-SCs [21, 30, 31]. These facts suggest that the dip-hump structure observed in both material families may be of the same origin, e.g. electron-spin-fluctuation interactions [3]. Note that spin fluctuations may extend to high energy in Fe-SCs [35]. However, the energy dependence of the electron-boson coupling $\alpha^2(\omega)$ may be the dominant factor determining the low energy resonance mode Ω_r , which leads to a pronounced peak in the pairing glue $\alpha^2 F(\omega)$ and is visible in the conductance spectra [36]. In conclusion, the dip-hump structure has been resolved by STM in the four major families of Fe-SCs and in two families of cuprates. These features link to the spin resonance Ω_r . The universal relation $\Omega \sim 4.8k_B T_c$ and $\Omega/2\Delta < 1$ suggests that the interactions of electrons with the spin resonance mode are crucial for the superconductivity in Fe-SCs.

3.2. Atomic impurities

Impurities in superconductors are an active subject of study, with the potential to unravel the pairing symmetry of the superconducting state. Impurities are particularly important in cuprates and Fe-SCs, most of which require chemical substitutions to enable superconductivity. While in conventional s -wave superconductors, only magnetic impurities cause pair-breaking and suppress superconductivity, in d -wave superconductors (e.g. cuprates) [37] and multi-band s_{\pm} wave superconductors (e.g. possibly Fe-SCs) [38, 39, 40, 41, 42, 43, 44], both magnetic and non-magnetic impurities are expected to induce bound states in the superconducting gap.

In Fe-SCs, intensive theoretical studies of single impurity effects have been performed since their discovery [38, 39, 40, 41, 42, 43, 44]. It was proposed that studies of single nonmagnetic impurity can address the ongoing debate between the s_{\pm} and s_{++} pairing symmetry, since most theoretical models suggest that only the sign change of the order parameter in s_{\pm} pairing can give rise to robust sub-gap bound states around non-magnetic impurities [39, 40, 42, 43, 44]. Therefore, spectroscopic study of the energetic structure of impurity-induced bound state resonances could constrain the pairing symmetry. Furthermore, STM study of the spatial structure of impurity-induced states

could address proposed phases such as orbital ordering which break the underlying crystal lattice symmetry [45, 46]. Exploration of single impurities is most promising in nominally stoichiometric superconductors with unreconstructed surfaces such as FeSe(001), $\text{KFe}_2\text{Se}_2(110)$, and $\text{LiFeAs}(001)$ [14, 47, 48].

Single atom impurities were first identified on stoichiometric FeSe films grown by molecular beam epitaxy (MBE) [14]. Both Fe adatoms and Se vacancies showed sub-gap resonances in dI/dV at symmetric energies, with more pronounced filled state peaks [Figs. 4(a)-4(c)]. These sub-gap resonances would indeed be expected at impurity sites for unconventional s_{\pm} wave pairing in FeSe [39, 40, 42, 43, 44]. However, the existence of resonances here does not prove the s_{\pm} pairing, as the magnetic nature of the impurities is unknown: if magnetic, they would possibly induce bound states even in the case of simple s -wave pairing [37].

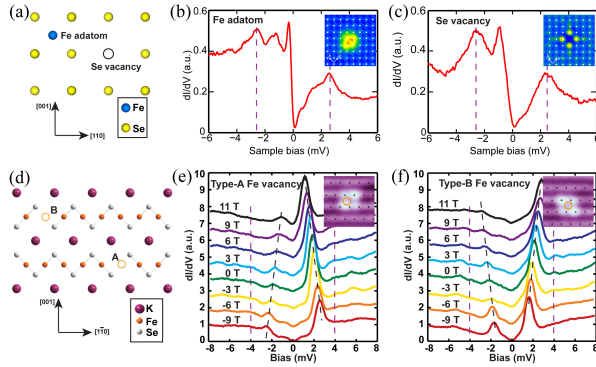


Figure 4: Impurity-induced bound states in the superconducting gaps of MBE-grown FeSe(001) and $\text{KFe}_2\text{Se}_2(110)$ films. (a-c) Schematic atomic structure of Fe adatom and Se vacancy, and their effects on the dI/dV spectra at 0.4 K. Insets show the corresponding topographic images ($3 \text{ nm} \times 3 \text{ nm}$, $V_s = 10 \text{ mV}$, $I = 0.1 \text{ nA}$) with white dots indicating the topmost Se atoms. Pronounced bound states were observed at -1.4 meV and -0.4 meV on Fe adatoms, and at -1.0 meV on Se vacancies. The tunnel junction was set at 10 mV and 0.1 nA [14]. (d-f) Atomic structure and magnetic-field dependence of dI/dV spectra measured on two inequivalent Fe vacancies at 0.4 K. Insets show the corresponding topographic images ($3 \text{ nm} \times 3 \text{ nm}$, $V_s = 30 \text{ mV}$, $I = 0.03 \text{ nA}$) with black dots indicating the K atoms. Black dashes depict the evolution of in-gap bound states with the applied magnetic field. The tunnel junction was set at 15 mV and 0.1 nA [47]. Megenta dashes indicate the energy positions for the superconducting gaps, as determined from spectra acquired at impurity-free regions.

Subsequently, Li *et al* introduced two types of mirror-symmetric Fe vacancies [Fig. 4(d)] into superconducting $\text{KFe}_2\text{Se}_2(110)$ films [47]. The dI/dV spectra on both impurities reveal strongly suppressed coherence peaks and a pair of in-gap resonances peaked at $\pm 1.9 \text{ mV}$ [Figs. 4(e) and 4(f)]. Although the energies

of the resonances at both sites are again symmetric with respect to E_F , their strengths are again quite different, but with more pronounced empty state peaks in contrast to FeSe [14]. More interestingly, the energies of the in-gap bound states on the two vacancies were found to shift linearly in opposite directions with applied magnetic field [Figs. 4(e) and 4(f)], demonstrating that the two Fe vacancies carry spins of different orientations. Therefore, the observed in-gap resonances do not contradict the theoretical predictions for either s_{\pm} or s_{++} pairing symmetry.

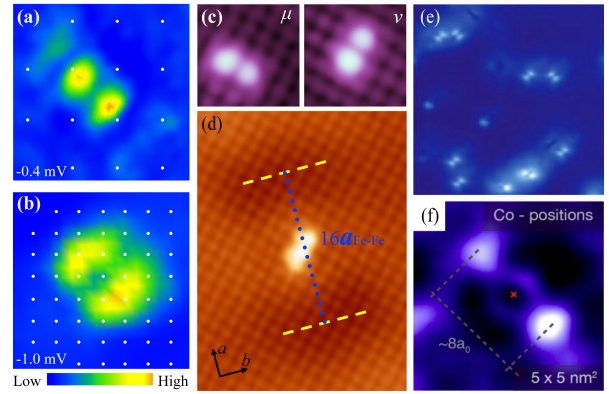


Figure 5: Symmetry breaking in Fe-SCs. (a, b) Bound states maps in the vicinity of single Fe adatom ($1.5 \text{ nm} \times 1.5 \text{ nm}$) and Se vacancy ($3 \text{ nm} \times 3 \text{ nm}$) of FeSe films [14]. The white dots indicate the topmost Se atoms. (c, d) Geometric ($2 \text{ nm} \times 2 \text{ nm}$, $V_s = 6 \text{ mV}$, $I = 0.1 \text{ nA}$) and electronic ($6 \text{ nm} \times 8 \text{ nm}$, $V_s = 10 \text{ mV}$, $I = 0.1 \text{ nA}$) dimers induced by the Se substitution for Fe sites in FeSe films [49]. (e) Geometric dimers in LiFeAs single crystals ($19 \text{ nm} \times 19 \text{ nm}$, $V_s = 20 \text{ mV}$, $I = 10 \text{ pA}$) lack accompanying electronic dimers [13]. (f) Average electronic dimer induced by Co substitution at the Fe site in $\text{Ca}(\text{Fe}_{0.97}\text{Co}_{0.03})_2\text{As}_2$ ($5 \text{ nm} \times 5 \text{ nm}$) [50].

Very recently, Grothe *et al* systematically characterized five predominant defects in nominally stoichiometric LiFeAs single crystals [48]. Despite their unknown chemical nature, these defects can be named according to their two-dimensional point group symmetries, and categorized into two distinct sets. One set consists of two different Fe- D_2 defects at the Fe sites, which preserve the local lattice symmetry, and exhibit only a single resonance near the edge of the smaller gap in this multi-gap superconductor. The other set, including Fe- C_2 , As- D_1 and Li- D_1 , was found to break the local lattice symmetry, and induce additional in-gap bound states, pronounced at either positive or negative biases. All five of these defects suppress the superconducting coherence peaks, and their in-gap resonances show such pronounced particle-hole asymmetry in the spectral weight that for some resonances no corresponding symmetric peak can

be detected on the opposite side of E_F . Although the magnetic nature of the impurities is unknown, one may speculate that some of the five may be non-magnetic, in which case the consistent existence of sub-gap resonances at all five different impurities would match theoretical predictions for s_{\pm} but not s_{++} pairing symmetry [39, 40, 42, 43, 44].

In addition to the bound state spectra of these impurities, which provide important information about pairing symmetry, the spatial structure of single atom defects, which often breaks the local lattice symmetry, supports the proposed orbital ordering phase [45, 46]. In FeSe, taking into account the full three-dimensional structure of each FeSe sheet, both Fe adatoms and Se vacancies have structural C_{4v} symmetry (aside from the unresolvably small 0.4% orthorhombicity [14]), yet both of their bound state dI/dV maps show pronounced C_{2v} symmetry [Figs. 5(a) and 3(b)]. This likely originates from an orbital ordering effect [14]. Furthermore, Se substitutions at the Fe site were also identified [49]. Although these defects produce stochastically oriented short-range “geometric dimer” signatures in keeping with the local C_{2v} symmetry of their lattice sites [Fig. 5(c)], they are also found to produce longer range a -axis-oriented electronic dimers with peaks separated by $\sim 16a_{\text{Fe-Fe}}$ [Fig. 5(d)].

The two orthogonal Fe- D_2 “geometric dimer” in LiFeAs [48] can be tentatively assigned to the two inequivalent Fe positions, by comparison to the analogous Se substitutions at Fe sites in FeSe films [49]. Interestingly, the Fe- D_2 impurities in LiFeAs do not appear to produce electronic dimers [Fig. 5(e)] [13], suggesting that neither orbital ordering [45, 46] nor pocket density wave ordering [51], both of which may give rise to such dimers, arises in the tetragonal phase of Fe-SCs such as LiFeAs.

Finally, although the density of Co dopants substituted at the Fe sites in orthorhombic $\text{Ca}(\text{Fe}_{0.97}\text{Co}_{0.03})_2\text{As}_2$ is too high to clearly distinguish special feature around individual Co atoms, an atomically registered averaging analysis recently showed that each dopant also forms an a -axis-oriented electronic dimer [Fig. 5(f)], similar to the electronic dimers in FeSe, but with peaks separated by 22 \AA , approximately $8a_{\text{Fe-Fe}}$ [50].

3.3. Normal state

STM spectroscopy was also used to probe the electronic structure of iron-based compounds in their parent and normal states. Most such studies have revealed a quite broad and asymmetric V-shaped DOS suppression around E_F [8], which is reminiscent of

the controversial pseudogap in cuprates [6]. In the case of iron-based materials, however, several other phenomena, such as surface reconstructions, or structural and magnetic transitions above T_c , may be responsible for the DOS suppression around E_F . It therefore appears more challenging to understand the DOS suppression in iron-based materials.

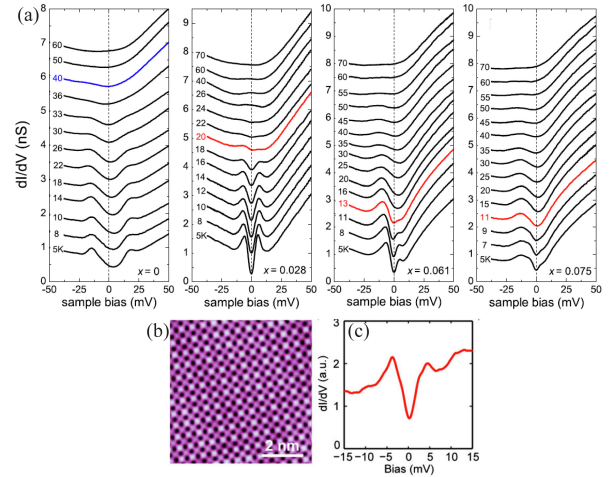


Figure 6: (a) Temperature dependence of dI/dV spectra in $\text{NaFe}_{1-x}\text{Co}_x\text{As}$ single crystals with various Co concentrations x . The blue (red) curve marks SDW (superconducting) transition. The curves are vertically offset for clarity [52]. (b, c) $\sqrt{2} \times \sqrt{2}$ charge ordering ($V_s = 40 \text{ mV}$, $I = 0.02 \text{ nA}$) and dI/dV spectrum in $\text{KFe}_2\text{Se}_2(001)$ films [53].

Zhou *et al* recently investigated the doping and temperature evolution of the electronic structure of 111-type $\text{NaFe}_{1-x}\text{Co}_x\text{As}$ single crystals by STM spectroscopy [Fig. 6] [52]. In the parent compound NaFeAs , temperature-dependent dI/dV spectra directly reveal a gap opening just below the spin density wave (SDW) transition temperature $T_{\text{SDW}} \sim 40 \text{ K}$. The observed gap edge peaks are consistent with the gap opening associated with a new electronic ordered state (such as superconductivity or SDW), where the DOS conservation will push states out toward the gap edge. In the case of the un-reconstructed surface of cleaved NaFeAs crystals, it is reasonably argued that the observed gap correlates closely with the SDW in the parent NaFeAs compound. Moreover, the SDW-related gap microscopically coexists and competes with the superconducting gap in an underdoped $\text{NaFe}_{1-x}\text{Co}_x\text{As}$ ($x=0.014$) sample, which lies at the SDW and superconducting phase boundary [54].

With increasing Co doping, the SDW gap is suppressed and an inhomogeneous superconducting gap occurs in optimally doped $\text{NaFe}_{1-x}\text{Co}_x\text{As}$ ($x=0.028$). In

contrast to cuprates, no pseudogap-like feature above T_c is found in the dI/dV spectra, similar to the doped $\text{FeSe}_{0.4}\text{Te}_{0.6}(001)$ [15] and stoichiometric $\text{FeSe}(001)$, $\text{LiFeAs}(001)$, and $\text{KFe}_2\text{Se}_2(110)$ surfaces [14, 13, 31, 47]. Unexpectedly, in overdoped $\text{NaFe}_{1-x}\text{Co}_x\text{As}$ ($x=0.061$ and 0.075), a spatially inhomogeneous pseudogap-like feature re-enters and persists to the relatively high temperature of 50 K. Since no gap edge peaks can be clearly observed at positive bias voltages up to 50 meV, it is not sufficiently convincing to claim that the DOS depression around E_F originates from yet another ordered state. The nature of the DOS depression in overdoped $\text{NaFe}_{1-x}\text{Co}_x\text{As}$ needs further investigation.

Using STM, Li *et al* imaged four different phases in MBE-grown $\text{KFe}_2\text{Se}_2(001)$ films on SrTiO_3 substrates. They argued that the parent compound corresponds to stoichiometric KFe_2Se_2 with $\sqrt{2} \times \sqrt{2}$ reconstruction with respect to the original Se lattice [Fig. 6(b)] [53], although this surface had previously been suggested to be superconducting due to the observed V-shaped gap by Cai *et al* [55]. However, the nonvanishing DOS(E_F) at 0.4 K [Fig. 6(c)] suggests that the V-shaped gap of Cai *et al* may have a non-superconducting origin [53]. Moreover, Cai *et al* explained the $\sqrt{2} \times \sqrt{2}$ reconstruction as the consequence of the block antiferromagnetic state of the underlying Fe layer [55]. Combining both studies, the V-shaped gap in the reconstructed $\sqrt{2} \times \sqrt{2}$ surface possibly originates from the SDW transition, similar to NaFeAs [52, 54].

4. Quasiparticle interference

In addition to inducing bound states, impurities can also scatter quasiparticles and lead to energy-dependent QPI patterns, which can be imaged in real space with spectroscopic STM [6, 8]. These patterns are then Fourier transformed to quantify the periodicity of electronic modulations. The combination of the real-space QPI pattern and momentum-space analysis is often called Fourier-transform scanning tunneling spectroscopy (FT-STs). Applications of FT-STs to cuprates have revealed dispersive or static electronic modulations in vortex cores, superconducting, and pseudogap states [6]. As a material enters into the superconducting state, its low-energy DOS redistributes according to the gap function Δ_k , such that the QPI patterns at these energies contain detailed information about the orbital structure of the superconducting order parameter [56]. Magnetic field-dependent FT-STs can even be used as a phase-sensitive probe to reveal the momentum-dependent coherence factors associated

with quasiparticle scattering and thus distinguish between different pairing symmetries in unconventional superconductors [15, 57].

In Fe-SCs, FT-STs may present richer QPI patterns due to the multiple Fermi surfaces derived from the five Fe d -orbitals [4]. STM on non-superconducting $\text{Ca}(\text{Fe}_{0.97}\text{Co}_{0.03})_2\text{As}_2$ gives evidence for static, unidirectional electronic nanostructures aligned along the crystalline a axis [16], which are further suggested to arise from the combined effects of all electronic dimers induced by Co substitutions at Fe sites [Fig. 5(f)] [50]. In fact, Song *et al* more directly observed similar electronic dimers induced by Se substitutions at Fe sites in superconducting FeSe films [Figs. 5(d)] [14, 49]. These findings provide evidence for the existence of a more complex electronic nematic state in the orthorhombic phase of some Fe-SCs, which may be responsible for the transport anisotropy in these materials [50, 58]. Anisotropy in Fe-SCs without Fe-site dopants remains to be understood.

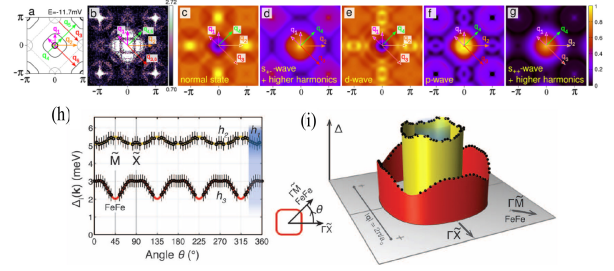


Figure 7: (a) Schematic constant energy contours (CECs) of LiFeAs at -11.7 meV with the dashes indicating the first Brillouin zone. There are two hole-like pockets around Γ and two electron-like pockets at the zone boundary. As marked, $q_{1...4}$ represent various scattering processes among the pockets, while $q_{5,6}$ represent umklapp processes. (b) Fourier transformed image of the measured QPI at the same energy as (a). The QPI features match well with the scattering $q_{1...6}$ vectors. (c-g) Calculated QPI (q space) in the normal and superconducting states with s_{\pm} , d , p , and s_{++} wave pairing symmetries [59]. (h) Anisotropic energy gap structure Δ_k on the three hole-like bands h_1 , h_2 , and h_3 of LiFeAs single crystal at $T = 1.2$ K. The 0.35 meV error represents the thermal resolution of FT-STs at 1.2 K. (i) Three-dimensional image of the measured Δ_k (solid dots) on the three hole-like bands [60]. Four-fold symmetric superconducting gaps are clearly visible with their minima aligned along ΓM ($\Gamma\bar{X}$) for h_3 (h_1 and h_2) band.

Recently, two groups performed FT-STs studies of LiFeAs , chosen for its clean and charge neutral cleaved surface [59, 60]. Hänke *et al* first found that the Fourier transformed QPI images closely resemble the LiFeAs Fermi surface itself [Figs. 7(a) and 7(b)]. The QPI images are then explained as a series of interband scattering processes between a small Γ -centered pocket (which acts like a van Hove

singularity) and other pockets [59]. This contrasts with most other Fe-SCs where the scattering between the well-matched hole and electron pockets plays a crucial role in both QPI patterns and s_{\pm} -wave pairing [15]. To determine the superconducting order parameter from their experimental QPI images, Hänke *et al* calculated the expected QPI in the superconducting state with various elementary order parameters (s_{++} , s_{\pm} , d and p waves) within the BCS model. They suggested that their data supported p wave pairing symmetry in LiFeAs, although a more complex order parameter such as $s + id$ wave could not be excluded. It should also be noted that the observation of a spin resonance in LiFeAs by neutron scattering does not support spin-triplet p -wave superconductivity in LiFeAs but instead suggests that the mechanism of superconductivity is similar to that in the other Fe-SCs [34].

Subsequently, Allan *et al* measured intraband QPI in LiFeAs to characterize the anisotropic superconducting energy gap Δ_k [60]. With much higher resolution than the previous experiment, they observed three distinct holelike Γ -centered bands h_1 , h_2 , and h_3 . At specific energies, the Fourier transformed images of Bogoliubov QPI $g(q, E)$ exhibit disconnected slices with vanishing scattering intensity in certain directions for each band, evidencing anisotropic Δ_k . Analysis shows that the gap minima correlate with the locus of maximum intensity in $g(q, E)$. Therefore, a plot of intensity maxima in a $g(q, E)$ plane along a high symmetry direction contains the information on Δ_k . Figures 7(c) and 7(d) summarize the experimental results. The superconducting energy gap Δ_k for the h_3 (h_1 and h_2) band shows four-fold symmetry with its minima aligned along $\Gamma\bar{M}$ ($\Gamma\bar{X}$) orientation. This differs from FeSe where two-fold pairing symmetry was suggested based on the anisotropic vortex structure [14].

5. Vortex State

Vortices, quantized tubes of magnetic flux, form as a magnetic field penetrates into a type-II superconductor. Since the pioneering work by Hess *et al* [61], STM has served as a powerful technique to visualize vortex arrangements in superconductors [6, 7, 8]. More significantly, STM can uniquely access the internal structure of a single vortex core, providing a measure of the superconducting coherence length ξ [10, 12] and even fundamental information about electron pairing [13, 14].

In 1964, Caroli *et al* theoretically predicted a series of quasiparticle bound states separated by $\sim \Delta^2/E_F$ within the vortex cores [62]. Since E_F is typically significantly

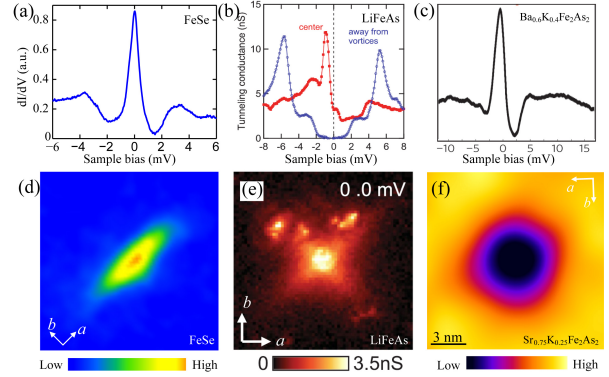


Figure 8: Vortex bound states and structure. (a-c) dI/dV spectra taken at the vortex center in (a) FeSe [14], (b) LiFeAs [13], (c) $\text{Ba}_{0.6}\text{K}_{0.4}\text{Fe}_2\text{As}_2$ [12]. (d-f) Vortex structure in (d) FeSe [14], (e) LiFeAs [13], (f) $\text{Sr}_{0.75}\text{K}_{0.25}\text{Fe}_2\text{As}_2$ [66]. White arrows mark the nearest Fe-Fe directions.

larger than Δ in conventional superconductors [63], the excitation spectra are quasi-continuous, and will appear as a pronounced peak at E_F , which can split into two symmetric peaks and eventually merge into the coherence peaks away from vortex center. This has been experimentally verified in NbSe_2 [61, 64]. In Fe-SCs, however, due to small carrier density (small E_F) and high T_c (large Δ) [4], Δ^2/E_F is relatively large and the excitation spectra are no longer continuous. Therefore, the quantum limit regime, where the DOS spectrum at the vortex center exhibit strong particle-hole asymmetry, may be anticipated [63, 65].

STM has revealed bound states within the vortex cores of stoichiometric FeSe [14] and LiFeAs [13], as well as hole-doped $\text{Ba}_{0.6}\text{K}_{0.4}\text{Fe}_2\text{As}_2$ [12]. In FeSe, Song *et al* observed a vortex core state exactly at E_F [Fig. 8(a)], which split into two symmetric peaks and eventually merged into the coherence peaks along the Fe-Fe orthorhombic b axis, analogous to the conventional superconductor NbSe_2 [64]. The splitting occurs along the Fe-Fe orthorhombic a axis as well, but the two symmetric peaks never merge into the coherence peaks, providing evidence of the two-fold symmetry in electron pairing. In contrast, STM studies of LiFeAs and $\text{Ba}_{0.6}\text{K}_{0.4}\text{Fe}_2\text{As}_2$ revealed significant particle-hole asymmetry in the DOS spectrum of the bound states, with pronounced peaks below E_F [Figs. 8(b) and 8(c)]. This suggests that LiFeAs and $\text{Ba}_{0.6}\text{K}_{0.4}\text{Fe}_2\text{As}_2$ may be located in the quantum limit regime.

In addition, STM conductance maps reveal material-dependent vortex core shapes. In FeSe, the vortex appears elongated along the a -axis [Fig.

8(d)], leading to the suggestion that the electron pairing is two-fold symmetric in FeSe [14]. In contrast, Hanaguri *et al* identified a four-fold star-shaped vortex in LiFeAs, with high LDOS tails oriented at 45° to the nearest Fe-Fe a and b axes [Fig. 8(e)] [13]. A model of gap anisotropy fails to account for the star-shaped vortex, because the gap minima in the outermost hole cylinder governing the LDOS distribution occur along the Fe-Fe directions [60, 67] and thus should give rise to high LDOS tails along a and b axes, in stark contrast to the experiments. To address this confusion, Wang *et al* theoretically calculated the shape of vortex cores by considering the Fermi surface anisotropy [68]. The results highlighted that the Fermi surface anisotropy can dominate the vortex core shape and prevent direct access of superconducting gap features if the gap itself is not highly anisotropic. Therefore, the observed four-fold star vortex core shape could be explained by the Fermi surface anisotropy in LiFeAs. Indeed, the ARPES experiment showed that the outermost hole cylinder exhibits a rounded square cross section with flat regions at 45° to the Fe-Fe directions in LiFeAs [67], which should lead to more quasiparticles and LDOS tails along these diagonals.

In nonstoichiometric Fe-SCs such as $\text{BaFe}_{1.8}\text{Co}_{0.2}\text{As}_2$ [10], $\text{Ba}_{0.6}\text{K}_{0.4}\text{Fe}_2\text{As}_2$ [12, 29], $\text{NaFe}_{0.975}\text{Co}_{0.025}\text{As}$ [29] and $\text{Sr}_{0.75}\text{K}_{0.25}\text{Fe}_2\text{As}_2$ [66], single vortices often appear irregularly shaped and it is challenging to identify the vortex structure. To overcome this issue, Song *et al* registered the vortex centers and then averaged the density of states from 48 vortices in $\text{Sr}_{0.75}\text{K}_{0.25}\text{Fe}_2\text{As}_2$ ($T_c=32$ K) [66], as depicted in Fig. 8(f). Although the underdoped $\text{Sr}_{0.75}\text{K}_{0.25}\text{Fe}_2\text{As}_2$ lies in the orthorhombic phase [4], the averaged vortex appears nearly isotropic, in contrast to the two- and four-fold symmetric vortices in FeSe and LiFeAs [13, 14]. This indeed supports the claim that the small orthorhombic lattice distortion can't bear the responsibility for the anisotropic vortices in FeSe [14]. Further experiments are needed to understand the internal structure of single vortices in doped Fe-SCs and their bearing on the pairing symmetry.

6. Conclusions

We have shown that in the past year the STM has made significant contributions in the quest for fundamental understanding of the microscopic electron pairing mechanism in Fe-SCs. Low temperature tunneling spectroscopy has revealed: (i) a generic dip-hump spectral feature beyond the superconducting gap in all four main structural families of Fe-SCs [14,

15, 27, 29, 30, 31], which links to the spin resonance detected by neutron scattering [29] and supports the importance of spin fluctuations in electron pairing in Fe-SCs; (ii) sub-gap bound states at single impurities in stoichiometric FeSe, LiFeAs and KFe_2Se_2 [14, 47, 48], consistent with a s_{\pm} wave electron pairing picture; (iii) rotational symmetry breaking in both parent and superconducting states [14, 16, 17, 50], supporting an orbital ordering phase in Fe-SCs [45, 46]; (iv) SDW-related gaps opening near E_F in the Fe-SC parent compounds [52, 54, 53, 55]. In addition to these achievements, QPI imaging has provided information about superconducting pairing symmetry [15, 59, 60], a prerequisite for the final determination of the nature of the high- T_c superconductivity in Fe-SCs. Finally, STM has directly imaged material-dependent vortex core states and shapes [12, 13, 14, 66]. Such results hint at the versatility in electron pairing, and can ultimately provide material-specific tests of the pairing symmetry in Fe-SCs.

Following these advances, there are a number of remaining questions to be addressed by the STM technique. In contrast to cuprates, the multi-band nature of Fe-SCs leads to electron pairing which relies sensitively on material and doping [4]. Even within the same material, the superconducting order parameter can change from nodal, in thick FeSe films on graphene [14], to nodeless, in single unit-cell FeSe films on SrTiO_3 [69]. The grandest challenge remains to clarify the pairing symmetry and its origin, as a prerequisite to understanding the secret of high- T_c superconductivity in Fe-SCs. Spectroscopy and QPI imaging serve as powerful techniques to extract the pairing symmetry. Meanwhile, spectroscopic imaging study of local DOS in the vicinity of both magnetic and non-magnetic impurities as well as vortices helps to distinguish between candidate pairing symmetries.

Another key issue is the role of dopants. For most Fe-SCs, particularly the higher- T_c 1111- and 122-type materials, the superconductivity develops from the parent compounds upon chemical doping of electrons, holes, or even isovalent elements. In addition to enabling superconductivity, the dopant atoms are also potential sources of scattering, nanoscale phase separation, and electronic inhomogeneity, which may in turn lead to transport anisotropy, T_c suppression, or vortex pinning. Therefore, STM can serve as an effective tool to probe these dopants on the nanometer scale and then understand their roles in superconductivity [50, 66].

Finally, we anticipate that STM will play a crucial role in finding higher- T_c materials. A number of

tantalizing hints of higher- T_c phases, such as 65 K T_c in single layer FeSe on a SrTiO₃ substrate [69, 70, 71] and 49 K T_c in $\sim 10\%$ volume fraction of Pr-doped CaFe₂As₂ [72, 73], have appeared in recent months. Just as STM served to disentangle the phase separation and identify the true chemical composition of the $T_c = 32$ K superconducting state in KFe₂Se₂ [47, 53], STM should be employed to find the minority volume fraction superconductivity in rare-earth-doped CaFe₂As₂. Such attempts in both Ca_{0.83}La_{0.17}Fe₂As₂ [74] and Ca_{1-x}Pr_xFe₂As₂ (where no clear superconducting gap is observed) [75] have so far been unsuccessful, but efforts are ongoing.

In conclusion, five years after the discovery of Fe-SCs, STM has contributed much to the understanding of these materials. Compared with the cuprates, Fe-SCs exhibit extraordinarily rich phenomenology, and can serve as a foil to unravel the secret of high- T_c superconductivity. There remain several important open questions, to which STM has the unique potential to provide answers.

Acknowledgement

We thank J. C. Davis and H.-H. Wen for helpful conversations. C. L. Song was supported by the Golub Fellowship at Harvard University.

References

- [1] Kamihara Y, Watanabe T, Hirano M, Hosono H. Iron-based layered superconductor LaO_{1-x}F_xFeAs ($x=0.05-0.12$) with $T_c=26$ K. *J Am Chem Soc* 2008;130:3296–7.
- [2] Ren ZA, Lu W, Yang J, Yi W, Shen XL, Li ZC, et al. Superconductivity at 55 K in iron-based F-doped layered quaternary compound SmO_{1-x}F_xFeAs. *Chin Phys Lett* 2008;25:2215–6.
- [3] Scalapino DJ. A common thread: The pairing interaction for unconventional superconductors. *Rev Mod Phys* 2012;84:1383–417.
- [4] Johnston DC. The puzzle of high temperature superconductivity in layered iron pnictides and chalcogenides. *Adv Phys* 2010;59:803–1061.
- [5] Stewart GR. Superconductivity in iron compounds. *Rev Mod Phys* 2011;83:1589–652.
- [6] Fischer Ø, Kugler M, Maggio-Aprile I, Berthod C, Renner C. Scanning tunneling spectroscopy of high-temperature superconductors. *Rev Mod Phys* 2007;79:353–419.
- [7] Yin Y, Zech M, Williams TL, Hoffman JE. Scanning tunneling microscopy and spectroscopy on iron-pnictides. *Physica C* 2009;469:535–44.
- [8] Hoffman JE. Spectroscopic scanning tunneling microscopy insights into Fe-based superconductors. *Rep Prog Phys* 2011;74:124513.
- [9] Tersoff J, Hamann DR. Theory and application for the scanning tunneling microscope. *Phys Rev Lett* 1983;50:1998–2001.
- [10] Yin Y, Zech M, Williams TL, Wang XF, Wu G, Chen XH, et al. Scanning tunneling spectroscopy and vortex imaging in the iron pnictide superconductor BaFe_{1.8}Co_{0.2}As₂. *Phys Rev Lett* 2009;102:97002.
- [11] Masee F, Huang Y, Huisman R, De Jong S, Goedkoop JB, Golden MS. Nanoscale superconducting-gap variations and lack of phase separation in optimally doped BaFe_{1.86}Co_{0.14}As₂. *Phys Rev B* 2009;79:220517.
- [12] Shan L, Wang YL, Shen B, Zeng B, Huang Y, Li A, et al. Observation of ordered vortices with andreev bound states in Ba_{0.6}K_{0.4}Fe₂As₂. *Nat Phys* 2011;7:325–31.
- [13] Hanaguri T, Kitagawa K, Matsubayashi K, Mazaki Y, Uwatoko Y, Takagi H. Scanning tunneling microscopy/spectroscopy of vortices in LiFeAs. *Phys Rev B* 2012;85:214505.
- [14] Song CL, Wang YL, Cheng P, Jiang YP, Li W, Zhang T, et al. Direct observation of nodes and twofold symmetry in FeSe superconductor. *Science* 2011;332:1410–3.
- [15] Hanaguri T, Niitaka S, Kuroki K, Takagi H. Unconventional s-wave superconductivity in Fe(Se,Te). *Science* 2010;328:474–6.
- [16] Chuang TM, Allan MP, Lee J, Xie Y, Ni N, Budko SL, et al. Nematic electronic structure in the parent state of the iron-based superconductor Ca(Fe_{1-x}Co_x)₂As₂. *Science* 2010;327:181–4.
- [17] Zhou XD, Ye C, Cai P, Wang XF, Chen XH, Wang YY. Quasiparticle interference of C₂-symmetric surface states in a LaOFeAs parent compound. *Phys Rev Lett* 2011;106:087001.
- [18] McMillan WL, Rowell JM. Lead phonon spectrum calculated from superconducting density of states. *Phys Rev Lett* 1965;14:108–12.
- [19] Renner CH, Fischer Ø. Vacuum tunneling spectroscopy and asymmetric density of states of Bi₂Sr₂CaCu₂O_{8+δ}. *Phys Rev B* 1995;51:9208–18.
- [20] DeWilde Y, Miyakawa N, Guptasarma P, Iavarone M, Ozyuzer L, Zasadzinski JF, et al. Unusual strong-coupling effects in the tunneling spectroscopy of optimally doped and overdoped Ba_{0.6}K_{0.4}Fe₂As₂. *Phys Rev Lett* 1998;80:153–6.
- [21] Zasadzinski JF, Ozyuzer L, Miyakawa N, Gray KE, Hinks DG, Kendziora C. Correlation of tunneling spectra in Bi₂Sr₂CaCu₂O_{8+δ} with the resonance spin excitation. *Phys Rev Lett* 2001;87:067005.
- [22] Niestemski FC, Kunwar S, Zhou S, Li S, Ding H, Wang Z, et al. A distinct bosonic mode in an electron-doped high-transition-temperature superconductor. *Nature* 2007;450:1058–61.
- [23] Fong HF, Bourges P, Sidis Y, Regnault LP, Ivanov A, Gu GD, et al. Neutron scattering from magnetic excitations in Bi₂Sr₂CaCu₂O_{8+δ}. *Nature* 1999;398:588–91.
- [24] Wilson SD, Dai P, Li S, Chi S, Kang HJ, Lynn JW. Resonance in the electron-doped high-transition-temperature superconductor Pr_{0.88}LaCe_{0.12}CuO_{4-δ}. *Nature* 2006;442:59–62.
- [25] Mazin II, Singh DJ, Johannes MD, Du MH. Unconventional superconductivity with a sign reversal in the order parameter of LaFeAsO_{1-x}F_x. *Phys Rev Lett* 2008;101:057003.
- [26] Kuroki K, Onari S, Arita R, Usui H, Tanaka Y, Kontani H, et al. Unconventional pairing originating from the disconnected fermi surfaces of superconducting LaFeAsO_{1-x}F_x. *Phys Rev Lett* 2008;101:087004.
- [27] Fasano Y, Maggio-Aprile I, Zhidadlo ND, Katrych S, Karpinski J, Fischer Ø. Local quasiparticle density of states of superconducting SmFeAsO_{1-x}F_x single crystals: Evidence for spin-mediated pairing. *Phys Rev Lett* 2010;105:167005.
- [28] Lee J, Fujita K, McElroy K, Slezak JA, Wang M, Aiura Y, et al. Interplay of electron-lattice interactions and superconductivity in Bi₂Sr₂CaCu₂O_{8+δ}. *Nature* 2006;442:546–50.
- [29] Wang ZY, Yang H, Fang DL, Shen B, Wang QH, Shan L, et al.

- Close relationship between superconductivity and the bosonic mode in $\text{Ba}_{0.6}\text{K}_{0.4}\text{Fe}_2\text{As}_2$ and $\text{NaFe}_{0.975}\text{Co}_{0.025}\text{As}$. *Nat Phys* 2013;9:42–8.
- [30] Shan L, Gong J, Wang YL, Shen B, Hou XY, Ren C, et al. Evidence of a spin resonance mode in the iron-based superconductor $\text{Ba}_{0.6}\text{K}_{0.4}\text{Fe}_2\text{As}_2$ from scanning tunneling spectroscopy. *Phys Rev Lett* 2012;108:227002.
- [31] Chi S, Grothe S, Liang R, Dosanjh P, Hardy WN, Burke SA, et al. Scanning tunneling spectroscopy of superconducting LiFeAs single crystals: Evidence for two nodeless energy gaps and coupling to a bosonic mode. *Phys Rev Lett* 2012;109:087002.
- [32] Christianson AD, Goremychkin EA, Osborn R, Rosenkranz S, Lumsden MD, Malliakas CD, et al. Unconventional superconductivity in $\text{Ba}_{0.6}\text{K}_{0.4}\text{Fe}_2\text{As}_2$ from inelastic neutron scattering. *Nature* 2008;456:930–2.
- [33] Balatsky AV, Zhu JX. Local strong-coupling pairing in d -wave superconductors with inhomogeneous bosonic modes. *Phys Rev B* 2006;74:094517.
- [34] Taylor A, Pitcher M, Ewings R, Perring T, Clarke S, Boothroyd A. Antiferromagnetic spin fluctuations in LiFeAs observed by neutron scattering. *Phys Rev B* 2011;83:220514.
- [35] Dai PC, Hu JP, Dagotto E. Magnetism and its microscopic origin in iron-based high-temperature superconductors. *Nat Phys* 2012;8:709–18.
- [36] Ahmadi O, Coffey L, Zasadzinski JF, Miyakawa N, Ozyuzer L. Eliashberg analysis of tunneling experiments: Support for the pairing glue hypothesis in cuprate superconductors. *Phys Rev Lett* 2011;106:167005.
- [37] Balatsky AV, Vekhter I, Zhu JX. Impurity-induced states in conventional and unconventional superconductors. *Rev Mod Phys* 2006;78:373–433.
- [38] Bang Y, Choi HY, Won H. Impurity effects on the $\pm s$ -wave state of the iron-based superconductors. *Phys Rev B* 2009;79:054529.
- [39] Zhang DG. Nonmagnetic impurity resonances as a signature of sign-reversal pairing in FeAs-based superconductors. *Phys Rev Lett* 2009;103:186402.
- [40] Tsai WF, Zhang YY, Fang C, Hu JP. Impurity-induced bound states in iron-based superconductors with s -wave $\cos k_x$ - $\cos k_y$ pairing symmetry. *Phys Rev B* 2009;80:064513.
- [41] Matsumoto M, Koga M, Kusunose H. Single impurity effects in multiband superconductors with different sign order parameters. *J Phys Soc Jpn* 2009;78:084718.
- [42] Ng TK, Avishai Y. In-gap bound states induced by nonmagnetic impurities in two-band s_{\pm} superconductors. *Phys Rev B* 2009;80:104504.
- [43] Kariyado T, Ogata M. Single-impurity problem in iron-pnictide superconductors. *J Phys Soc Jpn* 2010;79:083704.
- [44] Beaird R, Vekhter I, Zhu JX. Impurity states in multiband s -wave superconductors: Analysis of iron pnictides. *Phys Rev B* 2012;86:140507.
- [45] Lv W, Wu J, Phillips P. Orbital ordering induces structural phase transition and the resistivity anomaly in iron pnictides. *Phys Rev B* 2009;80:224506.
- [46] Lee CC, Yin WG, Ku W. Ferro-orbital order and strong magnetic anisotropy in the parent compounds of iron-pnictide superconductors. *Phys Rev Lett* 2009;103:267001.
- [47] Li W, Ding H, Deng P, Chang K, Song CL, He K, et al. Phase separation and magnetic order in K-doped iron selenide superconductor. *Nat Phys* 2011;8:126–30.
- [48] Grothe S, Chi S, Dosanjh P, Liang RX, Hardy WN, Burke SA, et al. Bound states of defects in superconducting LiFeAs studied by scanning tunneling spectroscopy. *Phys Rev B* 2012;86:174503.
- [49] Song CL, Wang YL, Jiang YP, Wang L, He K, Chen X, et al. Suppression of superconductivity by twin boundaries in FeSe . *Phys Rev Lett* 2012;109:137004.
- [50] Allan MP, Chuang TM, Masee F, Xie Y, Ni N, Bud'ko SL, et al. Anisotropic impurity-states, quasiparticle scattering and nematic transport in underdoped $\text{Ca}(\text{Fe}_{1-x}\text{Co}_x)_2\text{As}_2$. *Nat Phys* 2013;doi:10.1038/nphys2544.
- [51] Kang J, Tešanović Z. Dimer impurity scattering, reconstructed fermi-surface nesting, and density-wave diagnostics in iron pnictides. *Phys Rev B* 2012;85:220507.
- [52] Zhou X, Cai P, Wang AF, Ruan W, Ye C, Chen XH, et al. Evolution from unconventional spin density wave to superconductivity and a pseudogaplike phase in $\text{NaFe}_{1-x}\text{Co}_x\text{As}$. *Phys Rev Lett* 2012;109:037002.
- [53] Li W, Ding H, Li Z, Deng P, Chang K, He K, et al. KFe_2Se_2 is the parent compound of K-doped iron selenide superconductors. *Phys Rev Lett* 2012;109:057003.
- [54] Cai P, Zhou XD, Ruan W, Wang AF, Chen XH, Lee DH, et al. Visualizing the microscopic coexistence of spin density wave and superconductivity in underdoped $\text{NaFe}_{1-x}\text{Co}_x\text{As}$. *arXiv* 2012;1208.3842.
- [55] Cai P, Ye C, Ruan W, Zhou XD, Wang AF, Zhang M, et al. Imaging the coexistence of a superconducting phase and a charge-density modulation in the KFe_2Se_2 superconductor using a scanning tunneling microscope. *Phys Rev B* 2012;85:094512.
- [56] McElroy K, Simmonds RW, Hoffman JE, Lee DH, Orenstein J, Eisaki H, et al. Relating atomic-scale electronic phenomena to wave-like quasiparticle states in superconducting $\text{Ba}_{0.6}\text{K}_{0.4}\text{Fe}_2\text{As}_2$. *Nature* 2003;422:592–6.
- [57] Hanaguri T, Kohsaka Y, Ono M, Maltseva M, Coleman P, Yamada I, et al. Coherence factors in a high- T_c cuprate probed by quasi-particle scattering off vortices. *Science* 2009;323:923–6.
- [58] Chu JH, Analytis JG, De Greve K, McMahan PL, Islam Z, Yamamoto Y, et al. In-plane resistivity anisotropy in an underdoped iron arsenide superconductor. *Science* 2010;329:824–6.
- [59] Hänke T, Sykora S, Schlegel R, Baumann D, Harnagea L, Wurmehl S, et al. Probing the unconventional superconducting state of LiFeAs by quasiparticle interference. *Phys Rev Lett* 2012;108:127001.
- [60] Allan MP, Rost AW, Mackenzie AP, Xie Y, Davis JC, Kihou K, et al. Anisotropic energy gaps of iron-based superconductivity from intraband quasiparticle interference in LiFeAs . *Science* 2012;336:563–7.
- [61] Hess HF, Robinson RB, Dynes RC, Valles Jr JM, Waszczak JV. Scanning-tunneling-microscope observation of the abrikosov flux lattice and the density of states near and inside a fluxoid. *Phys Rev Lett* 1989;62:214–6.
- [62] Caroli C, De Gennes PG, Matricon J. Bound fermion states on a vortex line in a type II superconductor. *Phys Lett* 1964;9:307–9.
- [63] Shore JD, Huang M, Dorsey AT, Sethna JP. Density of states in a vortex core and the zero-bias tunneling peak. *Phys Rev Lett* 1989;62:3089–92.
- [64] Hess HF, Robinson RB, Waszczak JV. Vortex-core structure observed with a scanning tunneling microscope. *Phys Rev Lett* 1990;64:2711–4.
- [65] Hayashi N, Isoshima T, Ichioka M, Machida K. Low-lying quasiparticle excitations around a vortex core in quantum limit. *Phys Rev Lett* 1998;80:2921–4.
- [66] Song CL, Yin Y, Zech M, Williams T, Yee M, Chen GF, et al. Electronic inhomogeneity and vortex disorder in superconducting $\text{Sr}_{0.75}\text{K}_{0.25}\text{Fe}_2\text{As}_2$. *arXiv* 2012;1212.3240.
- [67] Umezawa K, Li Y, Miao H, Nakayama K, Liu ZH, Richard P, et al. Unconventional anisotropic s -wave superconducting

- gaps of the LiFeAs iron-pnictide superconductor. *Phys Rev Lett* 2012;108:037002.
- [68] Wang Y, Hirschfeld PJ, Vekhter I. Theory of quasiparticle vortex bound states in iron-based superconductors: Application to scanning tunneling spectroscopy of LiFeAs. *Phys Rev B* 2012;85:020506.
- [69] Wang QY, Li Z, Zhang WH, Zhang ZC, Zhang JS, Li W, et al. Interface induced high temperature superconductivity in single unit-cell fese films on SrTiO₃. *Chin Phys Lett* 2008;29:037402.
- [70] He SL, He JF, Zhang WH, Zhao L, Liu DF, Liu X, et al. Phase diagram and high temperature superconductivity at 65 K in tuning carrier concentration of single-layer FeSe films. *arXiv* 2012;1207.6823.
- [71] Tan SY, Xia M, Zhang Y, Ye ZR, Chen F, Xie X, et al. Interface-induced superconductivity and strain-dependent spin density wave in FeSe/SrTiO₃ thin films. *arXiv* 2013;1301.2748.
- [72] Lv B, Deng L, Gooch M, Wei F, Sun Y, Meen JK, et al. Unusual superconducting state at 49 K in electron-doped CaFe₂As₂ at ambient pressure. *Proc Nat Acad Sci* 2011;108:15705–9.
- [73] Saha SR, Butch NP, Drye T, Magill J, Ziemak S, Kirshenbaum K, et al. Structural collapse and superconductivity in rare-earth-doped CaFe₂As₂. *Phys Rev B* 2012;85:024525.
- [74] Huang YB, Richard P, Wang JH, Wang XP, Shi X, Xu N, et al. Experimental investigation of the electronic structure of CaFe₂As₂. *arXiv* 2012;1210.7288.
- [75] Zeljkovic I, Huang D, Song CL, Lv B, Chu CW, Hoffman JE. Nanoscale surface element identification and dopant homogeneity in the high-T_c superconductor Pr_xCa_{1-x}Fe₂As₂. *arXiv* 2013;1301.4942.